

1 Developmental differences in canonical cortical networks: insights from  
2 microstructure-informed tractography  
3

4 Sila Genc<sup>1,2,3\*</sup>, Simona Schiavi<sup>1,4,5\*</sup>, Maxime Chamberland<sup>1,6</sup>, Chantal Tax<sup>7,8</sup>, Erika Raven<sup>1,9</sup>,  
5 Alessandro Daducci<sup>4</sup>, Derek K Jones<sup>1</sup>

6  
7 <sup>1</sup>Cardiff University Brain Research Imaging Centre (CUBRIC), School of Psychology, Cardiff  
8 University, Cardiff, United Kingdom

9 <sup>2</sup> Neuroscience Advanced Clinical Imaging Service (NACIS), Department of Neurosurgery, The  
10 Royal Children's Hospital, Parkville, Victoria, Australia

11 <sup>3</sup> Developmental Imaging, Clinical Sciences, Murdoch Children's Research Institute, Parkville,  
12 Victoria, Australia

13 <sup>4</sup> Department of Computer Science, University of Verona, Italy

14 <sup>5</sup> ASG Superconductors S.p.A., Genova, Italy

15 <sup>6</sup> Eindhoven University of Technology, Department of Mathematics and Computer Science,  
16 Eindhoven, The Netherlands

17 <sup>7</sup> Image Sciences Institute, University Medical Center Utrecht, Utrecht, The Netherlands

18 <sup>8</sup> School of Physics, Cardiff University, UK

19 <sup>9</sup> Center for Biomedical Imaging, Department of Radiology, New York University Grossman School  
20 of Medicine, New York, USA

21

22 \*authors contributed equally

23 **Corresponding Author**

24 Sila Genc

25 Department of Neurosurgery  
26 Royal Children's Hospital  
27 Parkville, Victoria, Australia  
28 E: [sila.genc@mcri.edu.au](mailto:sila.genc@mcri.edu.au)

29 **Short title:** Developmental differences in microstructure-informed brain networks

30 **Keywords**

31 Development, connectivity, microstructure informed tractography, cortical, diffusion

32 **Abstract**

33 There is a growing interest in incorporating white matter fibre-specific microstructural properties  
34 into structural connectomes to obtain a more quantitative assessment of brain connectivity. In a  
35 developmental sample aged 8-18 years, we studied age-related patterns of microstructure-  
36 informed network properties locally and globally. First, we computed the diffusion-weighted signal  
37 fraction associated with each tractography-reconstructed streamline. Then, we generated  
38 microstructure-informed connectomes from diffusion MRI data using the convex optimization  
39 modelling for microstructure-informed tractography (COMMIT) approach. Finally, we estimated  
40 network characteristics in eight functionally defined networks (visual, somatomotor, dorsal  
41 attention, ventral attention, limbic, frontoparietal, default mode and subcortical networks). Our  
42 findings reveal that throughout child and adolescent development, global efficiency increases in  
43 the visual, somatomotor, and default mode networks, and mean strength increases in the  
44 somatomotor and visual networks. Nodes belonging to the dorsal and ventral visual pathways  
45 demonstrate the largest age-dependence in local efficiency, supporting previous evidence of  
46 protracted maturation of dorsal and ventral visual pathways. Our results provide compelling  
47 evidence that there is a prolonged development of visual association cortices.

48 **1. Introduction**

49

50 The transition from childhood to adolescence is a period of profound neurobiological and cognitive  
51 development where the human brain undergoes significant changes to refine neural substrates  
52 prior to adulthood (Blakemore & Choudhury, 2006). Essential to this process are the white matter  
53 pathways that form a structural scaffold facilitating connections and communication between  
54 cortical regions. Their development follows a stereotypical pattern of myelination, which closely  
55 mirrors the functional capacity of neural systems. For example, primary sensory, motor and visual  
56 pathways typically complete myelination by the first two years of life (Deoni et al., 2015), whereas  
57 frontal and temporal association regions continue to develop well into adulthood, with peak  
58 myelination happening in the second decade of life (Bartzokis et al., 2012; Yakovlev & Lecours,  
59 1967). The process of axonal development is less clear, with early *ex vivo* studies indicating  
60 stabilization of corpus callosum axonal count by six months of age (LaMantia & Rakic, 1990) and  
61 further work indicating changes to axonal and myelin properties at pubertal onset (Genc et al.,  
62 2023; Juraska & Willing, 2017; Paus, 2010).

63

64 Developmental studies using magnetic resonance imaging (MRI) have revealed that white matter  
65 volume steadily increases over childhood and adolescence (Giedd et al., 1999; Lenroot & Giedd,  
66 2006), likely by way of coupled radial growth of the axon and myelin sheath. In tandem, functional  
67 MRI (fMRI) studies suggest a greater degree of temporal network connectivity, which remodels  
68 from infancy to early adulthood (Grayson & Fair, 2017). Early in childhood, sensorimotor systems  
69 become well integrated and coordinated, and show little change into adulthood (Gu et al., 2015).  
70 Later in adolescence, functional hubs such as fronto-parietal, attentional and salience networks  
71 become increasingly segregated, allowing for flexibility as the adolescent brain becomes more  
72 adaptable to increase performance and efficiency (Bassett et al., 2011).

73

74 Diffusion magnetic resonance imaging (dMRI) has enabled novel discoveries in spatial and  
75 temporal patterns of white matter fibre development (Geeraert et al., 2019; Genc et al., 2018;  
76 Herting et al., 2017; Lebel & Beaulieu, 2011; Palmer et al., 2022; Tamnes et al., 2018). Structural  
77 connectivity has been studied using diffusion MRI tractography (Hagmann et al., 2007) to  
78 reconstruct white matter pathways or connections between nodes of interest (e.g., between  
79 distinct predefined cortical regions). Connection strength is commonly defined using white matter  
80 streamline count, i.e., the number of streamlines, derived from tractography, that run between  
81 nodes. However, this notion can be arbitrary, since streamline count is not biologically informative  
82 and can heavily depend on acquisition and processing parameters (Jones et al., 2013; Yeh et al.,  
83 2021; Zhang et al., 2022). Recent studies have attempted to improve the *status quo* in  
84 determining biologically informative determinants of connection strength using diffusion MRI  
85 (Smith et al., 2020; Zhang et al., 2022), however, the question remains: which measures are  
86 optimally informative?

87

88 To define more informative edge weights for the structural connectome, the 'tractometry'  
89 approach was introduced in (Bells et al., 2011; Jones et al., 2006; Kanaan et al., 2006) and

90 employed to study typical white matter development (Chamberland et al., 2019). This approach  
91 includes the mapping of microstructural measures along tractography-reconstructed pathways  
92 and computing average values for quantitative comparisons between measures. A challenge  
93 arises when multiple bundles pass through the same imaging voxel (an extremely prevalent  
94 phenomena; see Jeurissen et al. (2013); Schilling et al. (2022)) which leads to biased measures  
95 assigned to each constituent bundle (Schiavi et al., 2022). The Convex Optimization Modelling for  
96 Microstructure Informed Tractography (COMMIT) (Daducci et al., 2015; Daducci et al., 2013)  
97 approach address this problem by deconvolving specific microstructural features on each  
98 streamline to recover individual contributions to the measured signal. By replacing the commonly  
99 used streamline count with intra-axonal signal fraction (IASF), it offers a quantitative and more  
100 biologically informative assessment of brain connectivity (Bergamino et al., 2022; Gabusi et al.,  
101 2022; Schiavi et al., 2022; Schiavi, Ocampo-Pineda, et al., 2020; Schiavi, Petracca, et al., 2020).  
102

103 To investigate age-related differences in structural connectivity among various canonical or  
104 domain-specific networks, graph theory provides a powerful analytical tool (Fornito et al., 2016;  
105 Zhang et al., 2022). Graph theoretical analysis permits the computation of networks at different  
106 levels of organization (Fornito et al., 2016; Yeh et al., 2021), using measures classified as (i) local  
107 (quantifying properties of individual nodes), (ii) mesoscale (describing interconnected clusters of  
108 nodes); and (iii) global (describing whole-brain connectivity properties) (Fornito et al., 2016;  
109 Rubinov & Sporns, 2010). At the global scale, graph measures reveal how the brain's structural  
110 wiring facilitates information communication between distant regions and cognitive systems.  
111 While structurally connected regions can communicate directly, signal propagation between  
112 unconnected nodes requires a sequence of one or more intermediate connections (Zhang et al.,  
113 2022). Thus, investigating these measures across and between predefined cognitive systems  
114 during development can shed light on the structural mechanisms behind functional expression  
115 (Seguin et al., 2019).  
116

117 In this study, we construct microstructure-informed connectomes and study age-related patterns  
118 of local and global structural brain network properties in a typically developing sample aged 8-18  
119 years.  
120

## 121 **2. Materials and methods**

### 122 **2.1. Participants**

123  
124 We enrolled a sample of typically developing children and adolescents aged 8-18 years recruited  
125 as part of the Cardiff University Brain Research Imaging Centre (CUBRIC) Kids study, with ethical  
126 approval from the School of Psychology ethics committee at Cardiff University. Participants and  
127 their parents/guardians were recruited via public outreach events, and written informed consent  
128 was obtained from the primary caregiver of each child participating in the study. Adolescents aged  
129 16-18 years additionally provided written consent. Children were excluded from the study if they  
130 had non-removable metal implants, or a reported history of a major head injury or epilepsy. All

131 procedures were conducted in accordance with the Declaration of Helsinki. A total of 88 children  
132 (Mean age = 12.6, SD = 2.9 years) were included in the current study (46 female).

133

134 **2.2. MRI acquisition**

135

136 Images were acquired on a 3T Siemens Connectom system with ultra-strong (300 mT/m)  
137 gradients. As described in (Genc et al., 2020), the protocol comprised: (a) a 3D Magnetization  
138 Prepared Rapid Gradient Echo (MPRAGE) for structural segmentation (TE/TR = 2/2300ms; voxel  
139 size  $1 \times 1 \times 1 \text{ mm}^3$ ); (b) multi-shell dMRI acquisition (TE/TR = 59/3000 ms; voxel size =  $2 \times 2 \times 2 \text{ mm}^3$ )  
140 with  $b \in [500, 1200, 2400, 4000, 6000] \text{ s/mm}^2$  in 30, 30, 60, 60, 60 directions respectively and  
141 additional 14  $b = 0 \text{ s/mm}^2$  volumes. Diffusion MRI data were acquired in an anterior-posterior  
142 phase-encoding direction, with one additional posterior-anterior volume.

143

144 **2.3. MRI processing**

145

146 A summary of image processing steps is illustrated in Figure 1.  $T_1$ -weighted data were processed  
147 using FreeSurfer version 6.0 (<http://surfer.nmr.mgh.harvard.edu>) to derive a white matter mask  
148 and parcellate the cortical grey matter according to the Destrieux atlas (Destrieux et al., 2010).  
149 Next, we registered the Yeo functional atlas (Yeo et al., 2011) in MNI space to each individual  
150 subject's space using a non-linear transformation as implemented in FNIRT of FSL (Smith et al.,  
151 2004). This allowed us to obtain eight functionally relevant cortical canonical networks (herein  
152 referred to as "Yeo7") for further interrogation (visual, somatomotor, dorsal attention, ventral  
153 attention, limbic, frontoparietal, default mode network, subcortical). Subsequently, we grouped  
154 regions of interest (ROIs) from the Destrieux atlas into the eight Yeo atlas networks. To merge the  
155 two atlases within each subject, we employed a data-driven approach (see Baum et al. (2017)).  
156 Briefly, each parcellated brain region was assigned to one of eight canonical functional brain  
157 networks (Yeo et al., 2011) by considering the maximum number of voxels in the intersection  
158 between the masks. We ensured that the same overlap was confirmed in the homologous ROIs  
159 and for at least 80% of the enrolled subjects, discarding any Destrieux ROIs that did not meet  
160 these criteria. The final subdivision can be seen in Figure 2 and Table S2. Finally, we linearly-  
161 registered the  $T_1$ -weighted images and the corresponding parcellations on dMRI data using  
162 FLIRT (Jenkinson et al., 2002) with boundary-based optimization (Greve & Fischl, 2009).

163

164 Diffusion MRI data were pre-processed as detailed in Genc et al. (2020). Briefly the preprocessing  
165 pipeline involved FSL (Smith et al., 2004), MRtrix3 (Tournier et al., 2019), and ANTs (Avants et al.,  
166 2011) tools using the following steps: denoising (Veraart et al., 2016); slice-wise outlier detection  
167 (Sairanen et al., 2018); and correction for drift (Vos et al., 2017); motion, eddy, and susceptibility-  
168 induced distortions (Andersson et al., 2003; Andersson & Sotiroopoulos, 2016); Gibbs ringing  
169 artefact (Kellner et al., 2016); bias field (Tustison et al., 2010); and gradient non-uniformities  
170 (Glasser et al., 2013; Rudrapatna et al., 2021). We performed multi-shell multi-tissue constrained  
171 spherical deconvolution (MSMT-CSD; Jeurissen et al. (2014)) and generated a whole-brain

172 probabilistic tractogram seeding from the white matter comprising 3 million streamlines (Tournier  
173 et al., 2010).

174

175 We then applied COMMIT (Daducci et al., 2015, 2013) using a stick-zeppelin-ball model  
176 (Panagiotaki et al., 2012) to effectively filter out implausible connections while obtaining the intra-  
177 axonal signal fraction for each streamline, as described in Schiavi, Petracca, et al. (2020). For a set  
178 of fixed intra- and extra- axonal diffusivities, we assume that the IASF is constant along the  
179 streamline. To set the diffusivity parameters in COMMIT, we performed voxel-wise estimations in  
180 one younger participant (8-year-old female) and one older participant (17-year-old female). In the  
181 white matter, diffusivities had minimal variation between the younger and older participant (Table  
182 S1). As a result, for all subjects we set the following diffusivities  $d_{\text{par}}=d_{\text{par\_zep}}=1.7 \times 10^{-3} \text{ mm}^2/\text{s}$ ,  
183  $d_{\text{perp}}=0.61 \times 10^{-3} \text{ mm}^2/\text{s}$ ,  $d_{\text{iso}} \text{ in } [1.7, 3.0] \times 10^{-3} \text{ mm}^2/\text{s}$  for all participants.

184

185 For each subject, the connectomes were built using nodes from the individual T1-based Destrieux  
186 parcellation by assigning the total IASF associated to each bundle as edge-weights as in Schiavi,  
187 Petracca, et al. (2020) and Gabusi et al. (2022). Briefly, for each subject, the microstructure-  
188 informed connectomes (i.e., obtained using COMMIT weights reflecting IASF associated to each  
189 streamline as entries) were built using the GM parcellation described above and computing the  
190 weighted average intra-axonal signal contribution of each bundle:

191

$$192 a_{ij} = \frac{\sum_{k=1}^{N_{ij}} x_{ij}^k \cdot l_k}{\frac{\sum_{k=1}^{N_{ij}} l_k}{N_{ij}}}$$

193

194 where  $i, j$  are the indices of ROIs connected by the bundle,  $N_{ij}$  is bundle's number of streamlines,  
195  $x_{ij}^k$  is the weight of the streamline,  $k$ , obtained by COMMIT, and  $l_k$ , its length. In this way, each  
196 entry contained the total IASF associated to the bundle given by the weighted average of the  
197 streamline contribution multiplied by its length and divided by the average length of the bundle.

198

#### 199 **2.4. Network analysis**

200

201 To investigate the relationship between network characteristics and age, we used the Brain  
202 Connectivity Toolbox for Python (Rubinov & Sporns, 2010) to compute the following network  
203 measures:

204

- 205 • modularity (reflecting network segregation);
- 206 • global efficiency (corresponding to the average inverse shortest weighted-path length and  
207 inversely related to the characteristic path length);
- 208 • clustering coefficient (reflecting the degree to which the nodes tend to cluster together);  
209 and

210     • mean strength (corresponding to the average of all the nodal strengths, where the nodal  
211        strength is the sum of the weights of links connected to the node).

212

213    We computed these global network measures for the entire connectome, as well as within each  
214    subnetwork identified within the Yeo7 atlas.

215

## 216    2.5. Age-relationships

217    To investigate age-related patterns of network characteristics across the Yeo7 networks, we  
218    applied linear mixed effects modelling using lme4 (Bates et al., 2015) in R (RStudio v3.4.3). We  
219    built a linear model which included age (linear term), sex and Yeo7 network as predictors, with  
220    intracranial volume (ICV) included as a covariate. We examined four network characteristics  
221    (modularity, global efficiency, clustering coefficient, mean strength) and compared the fit of the  
222    standard linear model with alternative models that incorporated interaction terms. To identify the  
223    most appropriate model, we used the Akaike Information Criterion (AIC) (Akaike, 1974), selecting  
224    the model with the lowest AIC as the most parsimonious. Individual general linear models were  
225    run to determine age-related differences in specific network characteristics in all eight Yeo7  
226    networks. Evidence for an association was deemed statistically significant when  $p < .005$   
227    (Benjamin et al., 2018).

228

## 229    2.6. Feature importance

230

231    To identify locally important nodes that contribute to developmental patterns within networks  
232    (identified in section 2.5), we performed age-prediction using linear regression and ElasticNet  
233    regularization in scikit-learn (i.e., L1 and L2 penalties). We investigated feature importance using  
234    the ROIs comprised in each network for age-prediction of local efficiency. First, we randomly split  
235    the data into training and validation sets using an 80-20 ratio, resulting in 80% of the data being  
236    allocated for training purposes and the remaining 20% for model evaluation (total N=88: 70  
237    training; 18 testing). Then, we performed feature scaling to ensure that all variables were on a  
238    similar scale. To assess the generalization performance of the ElasticNet model and to prevent  
239    overfitting, we employed a 5-fold cross-validation approach. We performed a grid search to  
240    determine the optimal values for the L1 ratio ([0.1, 0.5, 0.7, 0.9, 0.95, 0.99, 1]) based on the  
241    regression coefficient ( $R^2$ ).

242

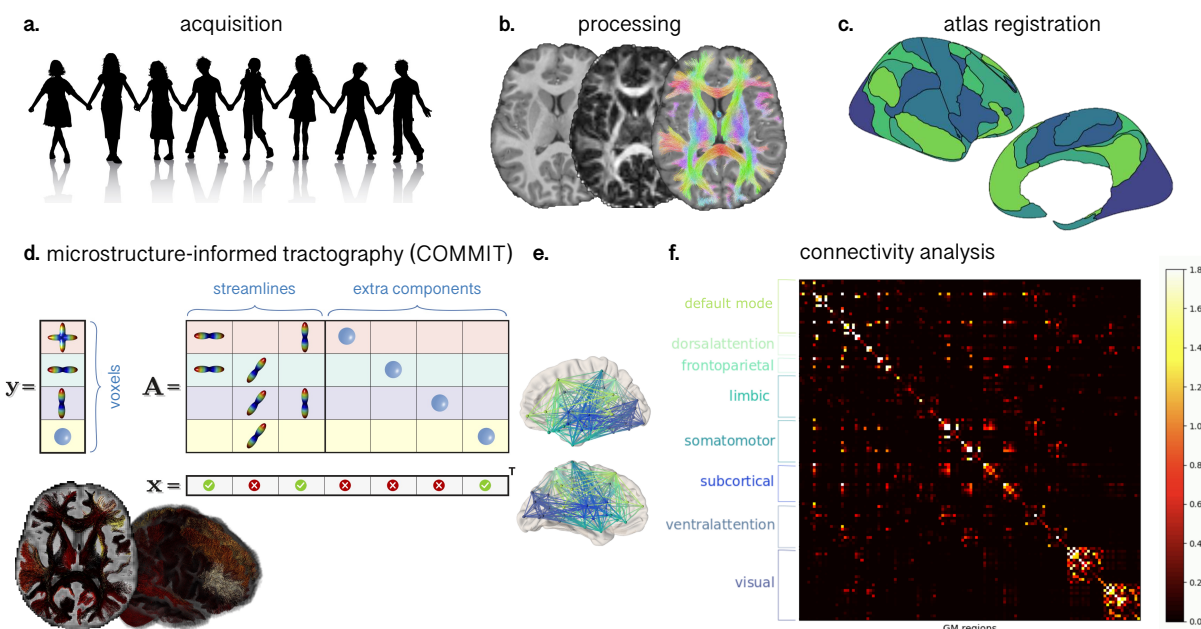
243    The performance of the model was assessed using the validation dataset. Finally, the features with  
244    the largest weight coefficients were extracted to identify specific cortical regions driving age-  
245    relationships in local network efficiency.

246

247

248

249



250

251 **Figure 1:** Workflow for constructing structural connectivity networks based on COMMIT derived  
 252 streamline weights: a) MRI data were acquired in 88 children and adolescents aged 8-18 years; b)  
 253 T1 and dMRI data were pre-processed; c) canonical cortical networks derived from a functional  
 254 atlas (Yeo et al., 2011) were co-registered to individual subject space; d) COMMIT (Daducci et al.,  
 255 2015, 2013) was applied using a stick-zeppelin-ball model to filter out implausible connections,  
 256 where computed weights reflect the intra-axonal signal fraction of each connection (brighter  
 257 values = higher IASF); e) interconnected nodes coloured by canonical cortical network; f)  
 258 connectivity matrix demonstrating connection strength between nodes within in each network  
 259 (brighter values = higher IASF).

260

261 **3. Results**

262

263 **3.1. Global network characteristics**

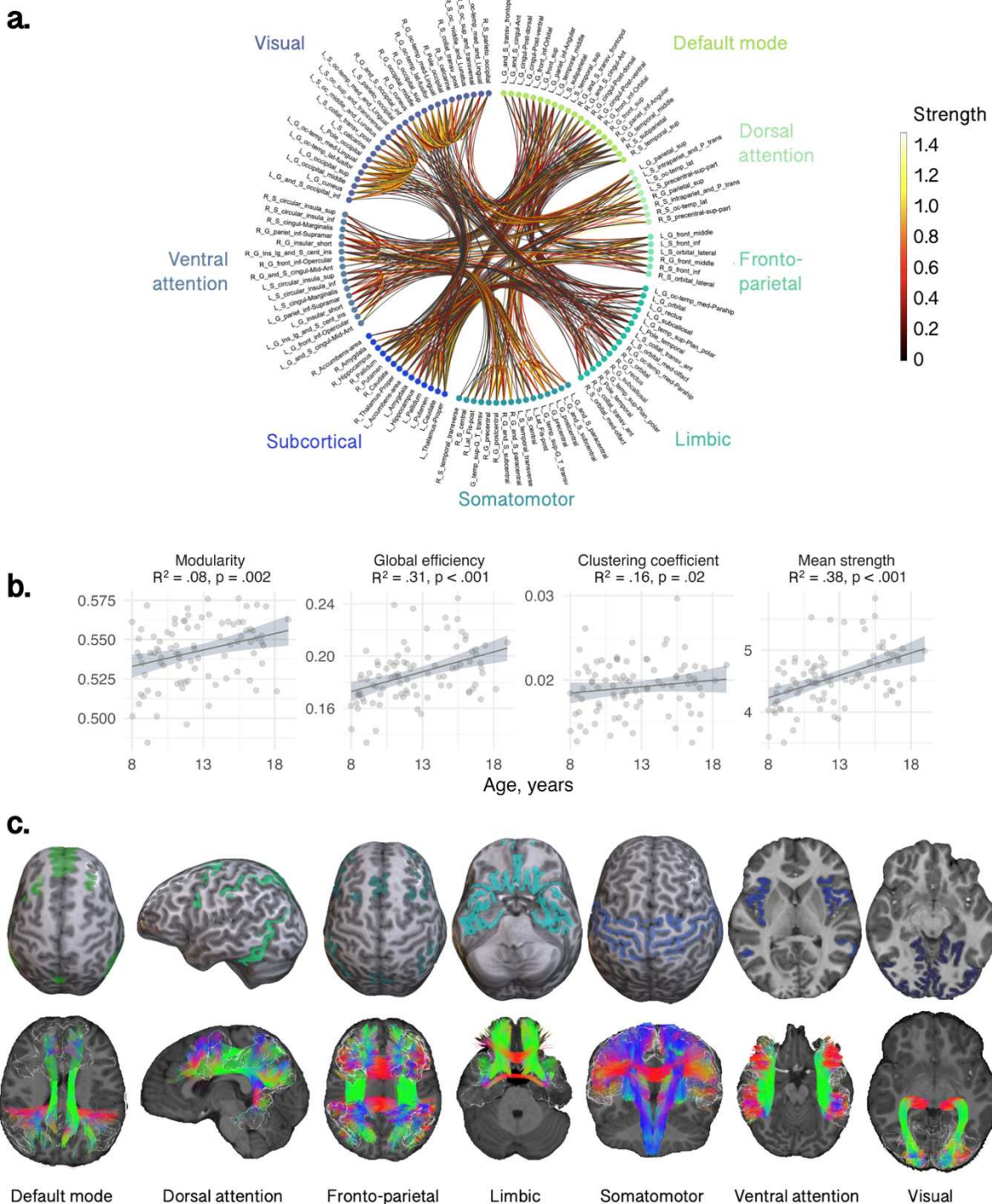
264

265 Linear models revealed a positive relationship between age and modularity ( $R^2 = .08, p = .002$ ),  
 266 global efficiency ( $R^2 = 0.31, p < 0.001$ ) and mean strength ( $R^2 = .38, p < .001$ ) (Figure 2b). The  
 267 relationship between age and clustering coefficient was not statistically significant ( $R^2 = .16, p =$   
 268  $.02$ ). As shown in the circle plot in Figure 2a, we also noted strong intra-regional connectivity and  
 269 strength within the visual and somatomotor networks, indicating robust interactions among  
 270 regions within these networks.

271

272 To test if specific networks were driving these developmental patterns of network properties, we  
 273 tested age-by-network interactions using a linear mixed effects model. The various models tested,  
 274 and the model selection results are summarised in Table S3. The best fitting model for all four  
 275 graph measures included an age by network by sex interaction term. We observed significant age-  
 276 by-network interactions in modularity ( $F = 6.6, p < .001$ ), global efficiency ( $F = 6.7, p < .001$ ),

277 clustering coefficient ( $F = 3.3, p = .002$ ), and mean strength ( $F = 23.9, p < .001$ ). As these results  
 278 indicated that there were age-related differences in network properties between the networks, we  
 279 performed subsequent analyses to test for age associations within networks, to discern whether  
 280 developmental patterns differed regionally. The various networks tested and their corresponding  
 281 anatomical tractography depictions are illustrated in Figure 2c.  
 282



283

284 **Figure 2:** Relationship between age and global network measures computed for the whole  
 285 connectome realized with Destrieux parcellation. a) The circle plot indicates the connection

286 strength between and within distinct networks obtained using the intra-axonal signal fraction  
287 estimated with COMMIT; b) Association between age and network characteristics between  
288 networks ( $R^2$  and p-value); c) Depiction of atlas-derived cortical functional networks and  
289 representative white matter tracts traversing these networks, for an 8-year-old female participant.

290

### 291 3.2. Sub-network characteristics

292

293 We identified regional differences in the age-related development of specific sub-networks (Table  
294 1 and Figure 3). Through linear regression analyses within individual networks, we found  
295 statistically significant relationships between age and global efficiency in the default mode ( $R^2 =$   
296 .38, p = .001), somatomotor ( $R^2 = .28$ , p < .001) and visual networks ( $R^2 = .43$ , p < .001). Clustering  
297 coefficient was positively associated with age in the visual network ( $R^2 = .37$ , p < .001). Moreover,  
298 age exhibited a positive association with mean strength in the somatomotor network ( $R^2 = .33$ , p <  
299 .001) and the visual network ( $R^2 = .46$ , p < .001). We also observed a negative association between  
300 age and modularity in the ventral attention network ( $R^2 = .13$ , p < .001). Overall, our results  
301 highlight the distinct age-related developmental patterns in the visual and somatomotor networks.

302

303 To confirm that the age-dependence of visual network properties were significantly different from  
304 other networks, we performed linear mixed-effects modelling to discern whether age-by-network  
305 interactions were significantly different between the visual network and the seven remaining sub-  
306 networks. Where the age-relationship in the visual network was significantly stronger than each  
307 subsequent network, this is summarised in Table S4 and annotated in Table 1. In summary, the  
308 most marked observations were in network strength, where the visual network had a significantly  
309 stronger age-dependency compared to each individual network, apart from the somatomotor  
310 network which also had a positive relationship with age.

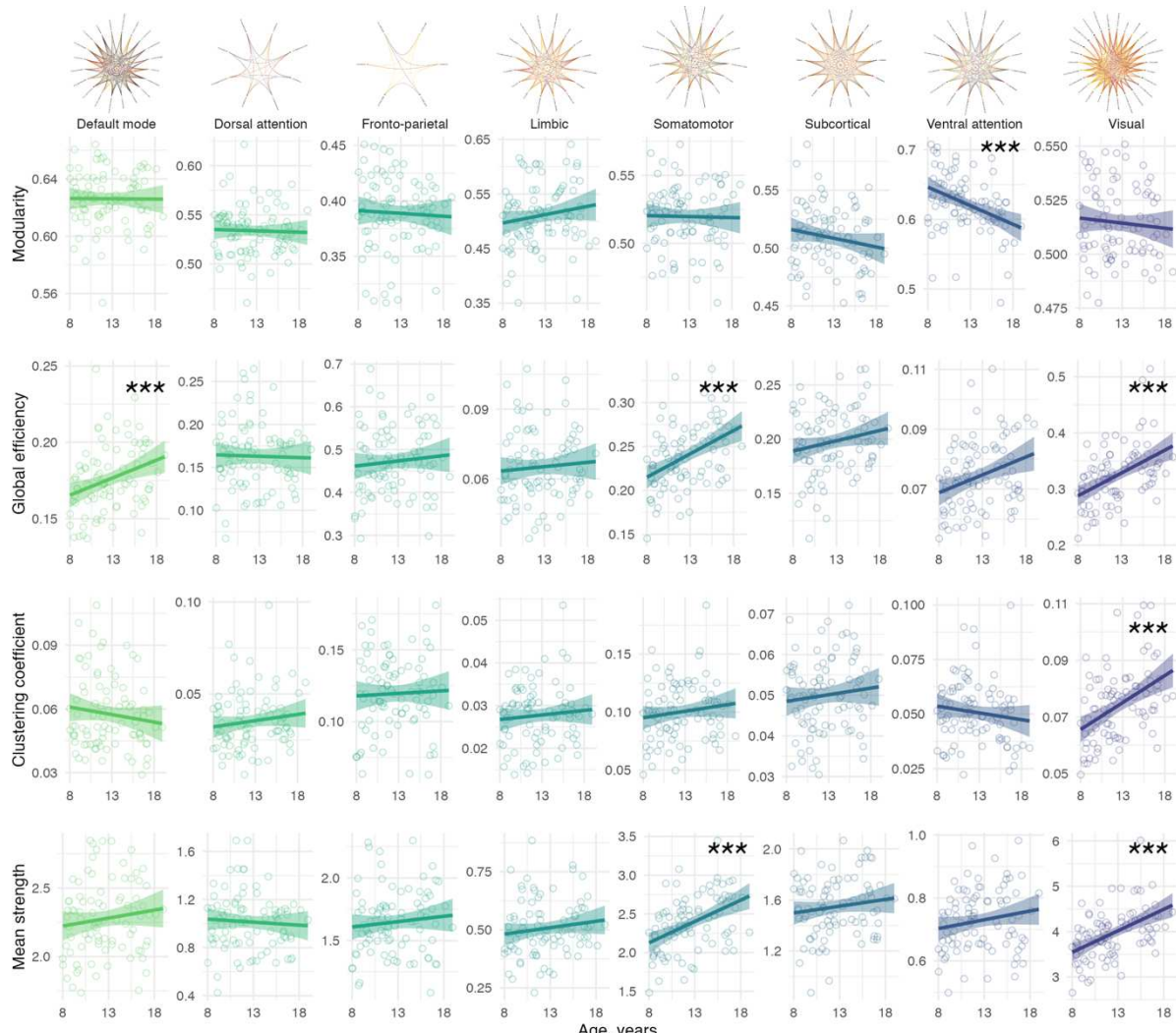
311

312 **Table 1:** Summary statistics for the relationship between age and global sub-network  
313 characteristics.

Network	Modularity		Global efficiency		Clustering coefficient		Mean strength	
	R <sup>2</sup>	p-value	R <sup>2</sup>	p-value	R <sup>2</sup>	p-value	R <sup>2</sup>	p-value
Default mode	.04	.55	.38	<b>.001</b>	.10	.59†	.43	.13†
Dorsal attention	-.03	.81	.06	.41†	.09	.20	.06	.23†
Fronto-parietal	.07	.66	.03	.58	-.01	.96	.07	.51†
Limbic	.07	.14	.19	.92	.14	.81	.21	.53†
Somatomotor	.01	.75	.28	<b>&lt;.001</b>	.30	.20	.33	<b>&lt;.001</b>
Subcortical	.08	.27	.03	.26	.01	.72	.02	.47†
Ventral attention	.13	<b>&lt;.001</b>	.19	.006	.11	.47†	.22	.12†
Visual	.11	.17	.43	<b>&lt;.001</b>	.37	<b>&lt;.001</b>	.46	<b>&lt;.001</b>

314 Note: Adjusted R<sup>2</sup> determined using a linear model including age, sex and total intracranial  
315 volume. Bold values indicate p<.005. † denotes a significant difference in the slope of the age  
316 relationship compared with the visual network.

317



318

319 **Figure 3:** Association between age and network properties within sub-networks. Significant age  
320 relationships are annotated (\*\*\*: p<.005). Top panel represents circle plots of within-network  
321 nodes, with brighter yellow connections indicative of higher mean strength.

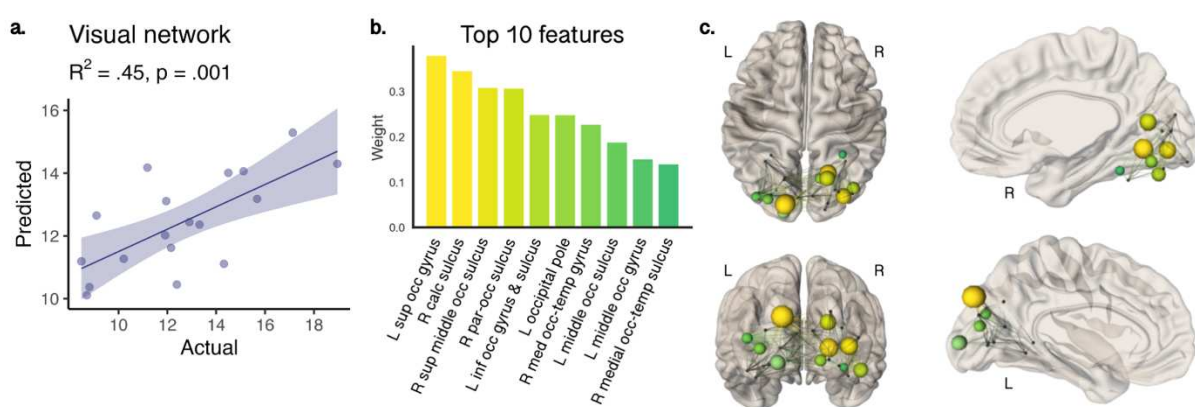
322

### 323 3.3. Feature importance of local efficiency

324

325 Age prediction of local efficiency in the visual network yielded a regression coefficient of 0.45  
326 (RMSE: 2.2, p=.001, Figure 4a) on the validation set (optimal value for L1=0.1). Feature  
327 importance in the visual network identified specific nodes (Figure 4) driving age-related increases  
328 in local efficiency. The 10 most sensitive nodes were balanced between hemispheres (5 nodes in  
329 right hemisphere, and 5 in the left) and accounted for 75% of variation in total weights (of a total of  
330 26 nodes). Figure 4b summarises the regions ranked by weight, and Figure 4c depicts these  
331 regions in axial, sagittal and coronal views in 3D. Nodes with high feature importance for age  
332 clustered together, including nodes which form the dorsal (left superior occipital gyrus and middle  
333 occipital gyrus and sulcus) and the ventral (right medial occipito-temporal sulcus and gyrus, and  
334 right lingual gyrus) visual pathways.

335  
336  
337  
338  
339  
340  
341  
342  
343  
344



345  
346  
347  
348  
349  
350  
351

**Figure 4:** Feature importance for age-prediction of local network efficiency in the visual cortex. A) predicted age was significantly associated with actual age; B) top 10 ranking regions that contributed most to age-related patterns displayed on C) axial, sagittal, and coronal glass brain views, where nodes are scaled and color-coded by weight. Nodes with high feature importance included left superior and middle occipital gyrus and right medial occipito-temporal gyrus.

352  
353

#### 4. Discussion

354  
355  
356  
357

We used microstructure-informed tractography to investigate global and local network characteristics in canonical cortical networks among a group of typically developing children and adolescents. Our study revealed three main findings:

358  
359  
360  
361  
362  
363  
364  
365  
366

First, whole-brain network-based measures of modularity, global efficiency and mean strength increased with age. This indicates that as children move through adolescence, the shortest path between nodes (in this case, regions from the Destrieux parcellation) decreases, resulting in a more efficient transfer of information. As a result, the nodes tend to cluster together to form hubs, and the strength of each connection increases with age. These findings align with known age-related increases in global efficiency during adolescent development (Baker et al., 2015; Khundrakpam et al., 2013; Koenis et al., 2018; Van den Heuvel & Sporns, 2013). Additionally, previous white matter studies have shown substantial increases in intra-axonal signal fraction with

367 age (Chang et al., 2015; Genc et al., 2020; Palmer et al., 2022), aligning with our observations of  
368 age-related increases in mean strength.

369

370 Second, sub-network analyses revealed specific networks with substantial age-related differences  
371 occurring from childhood to adolescence. In the default mode, somatomotor, and visual networks,  
372 global efficiency was higher with older age. Additionally, clustering coefficient was higher with age  
373 in the visual network, and mean strength was higher with age in the somatomotor and visual  
374 networks. Notably, brain structures, such as the primary visual and somatomotor cortex have  
375 highly organized and specialized structures that are closely related to their function, such as  
376 discriminating visual features (Wandell, 1999) and performing specific motor functions (Gordon et  
377 al., 2023). Together, our findings of age-related maturation of network efficiency and strength  
378 suggests a high degree of integration and communication within motor and visual processing  
379 regions, potentially reflecting the ongoing maturation of visual information processing and motor  
380 coordination capabilities during development. Our specific findings in the visual network align with  
381 previously observed temporal patterns of white matter microstructural maturation in the visual  
382 cortex (Colby et al., 2011; Genc et al., 2017) which are likely to be closely linked to age-related  
383 increases in axon density in humans (Genc et al., 2020) and rodents (Juraska & Willing, 2017).

384

385 Age-prediction in the visual cortex pointed to a smaller cluster of five regions per hemisphere that  
386 contributed to >75% of the observed age-related differences in local network efficiency. Our data  
387 driven approach suggests that nodes in the left dorsal (middle and superior occipital) visual  
388 pathway and the right ventral (middle occipito-temporal) visual pathway are driving developmental  
389 improvements in local network efficiency. The visual system undergoes early establishment during  
390 prenatal development and continues to mature through life (Gogtay et al., 2004; Knudsen, 2004).  
391 While myelination in the visual cortex is largely completed by the first year of life (Deoni et al.,  
392 2015), recent research indicates that myelination follows a protracted course in ventral temporal  
393 cortices (Natu et al., 2019). Ongoing intra-cortical myelination of the ventral temporal cortex may  
394 underlie MRI-derived estimates of cortical thinning, previously attributed to synaptic pruning  
395 (Gomez et al., 2017; Natu et al., 2019).

396

397 The maturation of association visual cortices supports higher level visual processing (e.g.  
398 recognising and discriminating objects, motion perception etc.) (Gomez et al., 2018). Our findings  
399 align with task-based fMRI studies involving object and shape recognition tasks, which  
400 demonstrate protracted development of dorsal and ventral visual pathways (Freud et al., 2019;  
401 Ward et al., 2023). These developmental improvements in shape-processing mechanisms likely  
402 contribute to microstructure-specific strengthening of global network efficiency and connection  
403 strength within the visual network through child and adolescent brain development. The age-  
404 related increases in local network efficiency in lateral temporo-occipital cortices may facilitate  
405 improvements in visual processing and function in these association cortices.

406

407 The myelination of these visual pathways may help to refine and optimize the neural connections  
408 and improve visual processing capabilities. Whilst we did not directly study myelination here, the

409 intra-axonal signal fraction explains a significant proportion of the age-related variance in network  
410 efficiency and connection strength. Taken together, our findings suggest that the visual cortex  
411 undergoes protracted development through childhood and adolescence. While our study primarily  
412 focuses on white matter microstructure for exploring graph-based measures, our observations of  
413 higher efficiency and connection strength with older age is predominantly due to ongoing  
414 microstructural maturation in the visual cortex.

415

#### 416 **4.1. Methodological advantages of the current approach**

417

418 We employed a data-driven approach to establish correspondence between a structural  
419 parcellation and functional atlas in each participant (Baum et al., 2017). This involved selecting  
420 the maximum number of voxels in the intersection between a smaller cortical region with its  
421 corresponding larger functional network. By ensuring that this overlap was consistent with the  
422 homologous ROIs and in at least 80% of the participants, we generated canonical cortical  
423 networks for the basis of regional graph-based analyses.

424

425 One of the significant advantages of the COMMIT framework is its ability to assign specific  
426 microstructural properties to individual tractography-reconstructed streamlines, which sets it apart  
427 from conventional (voxel-wise or vertex-wise) approaches where complex intra-voxel  
428 heterogeneity can bias estimates (Schilling et al., 2022). By allowing a distribution of  
429 microstructural values to be assigned to a voxel, i.e., the number of values is equal to the number  
430 of unique streamlines passing through the voxel and retained for analysis, COMMIT offers a more  
431 complete estimation of microstructural properties. In the context of graph theory, we are better  
432 equipped to capture the dynamic strengthening and weakening of connections with maturation  
433 over childhood and adolescence. Overall, the COMMIT framework offers a more nuanced and  
434 detailed characterization of microstructural properties along individual streamlines, countering  
435 complex intra-voxel heterogeneity, making it a powerful tool for a more meaningful assessment of  
436 brain connectivity (Gabusi et al., 2022; Schiavi et al., 2022; Schiavi, Ocampo-Pineda, et al., 2020;  
437 Schiavi, Petracca, et al., 2020).

438

#### 439 **4.2. Limitations and future directions**

440

441 It is important to acknowledge that certain functional networks utilised in our study here contain  
442 fewer nodes than others, potentially influencing our interpretations. Although we adopted a robust  
443 method to generate reproducible cortical nodes for each functional network, it resulted in some  
444 networks having a small number of nodes.

445

446 While there is a certain relationship between brain structure and function, structure-function  
447 coupling occurs in a spatially-dependent hierarchical manner (Baum et al., 2020). The brain is a  
448 complex and dynamic organ, with function influenced by a variety of factors, including structural  
449 organisation (Chamberland et al., 2017) and neural activity. Whilst the aforementioned factors

450 may help explain why we did not observe an age dependence of network-based measures of brain  
451 connectivity in regions known to remodel in adolescence (e.g. the fronto-parietal network), it is  
452 known that functional networks that are in close range demonstrate stronger white matter  
453 connectivity (Hermundstad et al., 2013), which may explain why our findings of global efficiency  
454 and mean strength were confined to the somatomotor and visual networks. On the note of the  
455 fronto-parietal network, despite running a ‘gold-standard’ dMRI pre-processing pipeline,  
456 susceptibility-induced distortion artefacts may introduce an additional source of variance into the  
457 diffusion MRI data, especially in fronto-parietal regions with an air/bone interface such as the nasal  
458 cavity.

459

460 Future work characterising the developing connectome using biologically meaningful  
461 mathematical models of brain connections are promising (Akarca et al., 2023; Seguin et al., 2023).  
462 Combining task-based or resting-state fMRI with microstructure-informed connectomes may  
463 better elucidate structure-function coupling across the developing brain (Suárez et al., 2020).  
464 Recent updates to the COMMIT framework offer the opportunity to incorporate additional imaging  
465 contrasts, such as myelin-sensitive contrasts, leading to improved delineation of anatomically  
466 accurate whole-brain tractography (Leppert et al., 2023; Schiavi et al., 2022).

467

## 468 5. Conclusion

469

470 Incorporating microstructural information into network analyses has shed light on distinct regional  
471 age-related development of brain networks. Notably, we observed unique characteristics within  
472 the visual network throughout development, supporting its ongoing maturation, reaffirming  
473 previously reported patterns of protracted development in the dorsal and ventral visual pathways.  
474 Overall, our study demonstrates the power of microstructure-informed tractography to decipher  
475 intricate developmental patterns, reinforcing the potential for deepening our understanding of  
476 brain connectivity and development.

477 **6. Supporting information**

478

479 **Acknowledgments**

480 We are grateful to the participants and their families for their participation in this study. We thank  
481 Umesh Rudrapatna and John Evans for their support with image acquisition protocols, Isobel  
482 Ward for assistance with data collection, Joseph Yang for scientific discussions, and Greg Parker  
483 for contributions to data pre-processing and model fitting pipelines. Image credit (Figure 1a) by  
484 kjpargeter on Freepik.

485 **Funding**

486

487 The data were acquired at the UK National Facility for In Vivo MR Imaging of Human Tissue  
488 Microstructure funded by the EPSRC (grant EP/M029778/1), and The Wolfson Foundation.  
489 SS received funding from the University of Verona Internationalisation Programme 2019 (Action  
490 4C). This research was funded in whole, or in part, by a Wellcome Trust Investigator Award  
491 (096646/Z/11/Z) and a Wellcome Trust Strategic Award (104943/Z/14/Z). CMWT was supported  
492 by a Veni grant (17331) from the Dutch Research Council (NWO) and the Wellcome Trust  
493 [215944/Z/19/Z]. For the purpose of open access, the author has applied a CC BY public  
494 copyright licence to any Author Accepted Manuscript version arising from this submission.

495 **Authors' Contributions**

496 S.S., S.G. and D.K.J. conceptualized the problem. S.S., S.G., M.C. and C.T. analyzed the MRI data.  
497 S.G. and E.R. acquired all MRI data. S.G and M.C. performed statistical analyses. A.D. and D.J.,  
498 supervised and raised funding for this project. S.S., S.G. and D.K.J. wrote the original draft of the  
499 manuscript. S.S., S.G., M.C., C.T., E.R., A.D., and D.K.J. reviewed and edited the manuscript.

500 **Code and data availability**

501 The code for COMMIT is open source and freely available at

502 <https://github.com/daducci/COMMIT>.

503 **Disclosures**

504 Declarations of interest: SG, MC, CT, ER, AD, DKJ declare no conflict of interest. SS is employed  
505 by ASG Superconductors S.p.A. but there is no financial interest related to this work.  
506

507 **7. References**

508

509

510 Akaike, H. (1974). A new look at the statistical model identification. *IEEE Transactions on*  
511 *Automatic Control*, 19(6), 716-723. <https://doi.org/10.1109/TAC.1974.1100705>

512 Akarca, D., Schiavi, S., Achterberg, J., Genc, S., Jones, D., & Astle, D. (2023). A weighted  
513 generative model of the human connectome. *bioRxiv*, 2023.2006.2023.546237.  
514 <https://doi.org/10.1101/2023.06.23.546237>

515 Andersson, J. L., Skare, S., & Ashburner, J. (2003). How to correct susceptibility distortions in  
516 spin-echo echo-planar images: application to diffusion tensor imaging. *NeuroImage*, 20(2),  
517 870-888.

518 Andersson, J. L. R., & Sotiroopoulos, S. N. (2016). An integrated approach to correction for off-  
519 resonance effects and subject movement in diffusion MR imaging. *NeuroImage*, 125,  
520 1063-1078. <https://doi.org/10.1016/j.neuroimage.2015.10.019>

521 Avants, B. B., Tustison, N. J., Song, G., Cook, P. A., Klein, A., & Gee, J. C. (2011). A reproducible  
522 evaluation of ANTs similarity metric performance in brain image registration. *NeuroImage*,  
523 54(3), 2033-2044.

524 Baker, S. T., Lubman, D. I., Yücel, M., Allen, N. B., Whittle, S., Fulcher, B. D., Zalesky, A., & Fornito,  
525 A. (2015). Developmental changes in brain network hub connectivity in late adolescence.  
526 *Journal of Neuroscience*, 35(24), 9078-9087.

527 Bartzokis, G., Lu, P. H., Heydari, P., Couvrette, A., Lee, G. J., Kalashyan, G., Freeman, F., Grinstead,  
528 J. W., Villablanca, P., Finn, J. P., Mintz, J., Alger, J. R., & Altshuler, L. L. (2012). Multimodal  
529 magnetic resonance imaging assessment of white matter aging trajectories over the  
530 lifespan of healthy individuals. *Biol Psychiatry*, 72(12), 1026-1034.  
531 <https://doi.org/10.1016/j.biopsych.2012.07.010>

532 Bassett, D. S., Wymbs, N. F., Porter, M. A., Mucha, P. J., Carlson, J. M., & Grafton, S. T. (2011).  
533 Dynamic reconfiguration of human brain networks during learning. *Proceedings of the  
534 National Academy of Sciences*, 108(18), 7641-7646.

535 Bates, D., Kliegl, R., Vasishth, S., & Baayen, H. (2015). Parsimonious mixed models. *arXiv preprint  
536 arXiv:1506.04967*.

537 Baum, G. L., Ceric, R., Roalf, D. R., Betzel, R. F., Moore, T. M., Shinohara, R. T., Kahn, A. E.,  
538 Vandekar, S. N., Rupert, P. E., Quarmley, M., Cook, P. A., Elliott, M. A., Ruparel, K., Gur, R.  
539 E., Gur, R. C., Bassett, D. S., & Satterthwaite, T. D. (2017). Modular Segregation of  
540 Structural Brain Networks Supports the Development of Executive Function in Youth.  
541 *Curr Biol*, 27(11), 1561-1572.e1568. <https://doi.org/10.1016/j.cub.2017.04.051>

542 Baum, G. L., Cui, Z., Roalf, D. R., Ceric, R., Betzel, R. F., Larsen, B., Cieslak, M., Cook, P. A., Xia, C.  
543 H., Moore, T. M., Ruparel, K., Oathes, D. J., Alexander-Bloch, A. F., Shinohara, R. T.,  
544 Raznahan, A., Gur, R. E., Gur, R. C., Bassett, D. S., & Satterthwaite, T. D. (2020).  
545 Development of structure–function coupling in human brain networks during youth.  
546 *Proceedings of the National Academy of Sciences*, 117(1), 771-778.  
547 <https://doi.org/10.1073/pnas.1912034117>

548 Bells, S., Cercignani, M., Deoni, S., Assaf, Y., Pasternak, O., Evans, C., Leemans, A., & Jones, D.  
549 (2011). Tractometry—comprehensive multi-modal quantitative assessment of white matter  
550 along specific tracts. *Proc. ISMRM*,

551 Benjamin, D. J., Berger, J. O., Johannesson, M., Nosek, B. A., Wagenmakers, E. J., Berk, R., Bollen,  
552 K. A., Brembs, B., Brown, L., Camerer, C., Cesarini, D., Chambers, C. D., Clyde, M., Cook, T.  
553 D., De Boeck, P., Dienes, Z., Dreber, A., Easwaran, K., Efferson, C., Fehr, E., Fidler, F., Field,  
554 A. P., Forster, M., George, E. I., Gonzalez, R., Goodman, S., Green, E., Green, D. P.,  
555 Greenwald, A. G., Hadfield, J. D., Hedges, L. V., Held, L., Hua Ho, T., Hoijtink, H., Hruschka,  
556 D. J., Imai, K., Imbens, G., Ioannidis, J. P. A., Jeon, M., Jones, J. H., Kirchler, M., Laibson, D.,  
557 List, J., Little, R., Lupia, A., Machery, E., Maxwell, S. E., McCarthy, M., Moore, D. A., Morgan,  
558 S. L., Munafó, M., Nakagawa, S., Nyhan, B., Parker, T. H., Pericchi, L., Perugini, M., Rouder,  
559 J., Rousseau, J., Savalei, V., Schönbrodt, F. D., Sellke, T., Sinclair, B., Tingley, D., Van  
560 Zandt, T., Vazire, S., Watts, D. J., Winship, C., Wolpert, R. L., Xie, Y., Young, C., Zinman, J.,  
561 & Johnson, V. E. (2018). Redefine statistical significance. *Nature Human Behaviour*, 2(1),  
562 6-10. <https://doi.org/10.1038/s41562-017-0189-z>

563 Bergamino, M., Schiavi, S., Daducci, A., Walsh, R. R., & Stokes, A. M. (2022). Analysis of brain  
564 structural connectivity networks and white matter integrity in patients with mild cognitive  
565 impairment. *Frontiers in Aging Neuroscience*, 14, 793991.

566 Blakemore, S. J., & Choudhury, S. (2006). Development of the adolescent brain: implications for  
567 executive function and social cognition. *Journal of child psychology and psychiatry*, 47(3-  
568 4), 296-312.

569 Chamberland, M., Girard, G., Bernier, M., Fortin, D., Descoteaux, M., & Whittingstall, K. (2017). On  
570 the Origin of Individual Functional Connectivity Variability: The Role of White Matter  
571 Architecture. *Brain Connectivity*, 7(8), 491-503. <https://doi.org/10.1089/brain.2017.0539>

572 Chamberland, M., Raven, E. P., Genc, S., Duffy, K., Descoteaux, M., Parker, G. D., Tax, C. M. W., &  
573 Jones, D. K. (2019). Dimensionality reduction of diffusion MRI measures for improved  
574 tractometry of the human brain. *NeuroImage*, 200, 89-100.  
<https://doi.org/10.1016/j.neuroimage.2019.06.020>

575 Chang, Y. S., Owen, J. P., Pojman, N. J., Thieu, T., Bukshpun, P., Wakahiro, M. L. J., Berman, J. I.,  
576 Roberts, T. P. L., Nagarajan, S. S., Sherr, E. H., & Mukherjee, P. (2015). White Matter  
577 Changes of Neurite Density and Fiber Orientation Dispersion during Human Brain  
578 Maturation. *PLOS ONE*, 10(6), e0123656. <https://doi.org/10.1371/journal.pone.0123656>

579 Colby, J. B., Van Horn, J. D., & Sowell, E. R. (2011). Quantitative in vivo evidence for broad regional  
580 gradients in the timing of white matter maturation during adolescence. *NeuroImage*, 54(1),  
581 25-31. <https://doi.org/https://doi.org/10.1016/j.neuroimage.2010.08.014>

582 Daducci, A., Dal Palù, A., Lemkadem, A., & Thiran, J. P. (2015). COMMIT: Convex optimization  
583 modeling for microstructure informed tractography. *IEEE Trans Med Imaging*, 34(1), 246-  
584 257. <https://doi.org/10.1109/tmi.2014.2352414>

585 Daducci, A., Palù, A. D., Lemkadem, A., & Thiran, J. P. (2013, 7-11 April 2013). A convex  
586 optimization framework for global tractography. 2013 IEEE 10th International Symposium  
587 on Biomedical Imaging,

588 Deoni, S. C. L., Dean, D. C., Remer, J., Dirks, H., & O'Muircheartaigh, J. (2015). Cortical maturation  
589 and myelination in healthy toddlers and young children. *NeuroImage*, 115, 147-161.  
<https://doi.org/https://doi.org/10.1016/j.neuroimage.2015.04.058>

590 Destrieux, C., Fischl, B., Dale, A., & Halgren, E. (2010). Automatic parcellation of human cortical  
591 gyri and sulci using standard anatomical nomenclature. *NeuroImage*, 53(1), 1-15.

592 Fornito, A., Zalesky, A., & Bullmore, E. (2016). *Fundamentals of brain network analysis*. Academic  
593 press.

594 Freud, E., Plaut, D. C., & Behrmann, M. (2019). Protracted Developmental Trajectory of Shape  
595 Processing along the Two Visual Pathways. *J Cogn Neurosci*, 31(10), 1589-1597.  
[https://doi.org/10.1162/jocn\\_a\\_01434](https://doi.org/10.1162/jocn_a_01434)

596 Gabusi, I., Pontillo, G., Petracca, M., Battocchio, M., Bosticardo, S., Costabile, T., Daducci, A., Pane,  
597 C., Riccio, E., & Pisani, A. (2022). Structural disconnection and functional reorganization in  
598 Fabry disease: a multimodal MRI study. *Brain Communications*, 4(4), fcac187.

599 Geeraert, B. L., Lebel, R. M., & Lebel, C. (2019). A multiparametric analysis of white matter  
600 maturation during late childhood and adolescence. *Human Brain Mapping*, 0(0).  
<https://doi.org/10.1002/hbm.24706>

601 Genc, S., Raven, E. P., Drakesmith, M., Blakemore, S.-J., & Jones, D. K. (2023). Novel insights into  
602 axon diameter and myelin content in late childhood and adolescence. *Cerebral Cortex*,  
603 33(10), 6435-6448. <https://doi.org/10.1093/cercor/bhac515>

604 Genc, S., Seal, M. L., Dhollander, T., Malpas, C. B., Hazell, P., & Silk, T. J. (2017). White matter  
605 alterations at pubertal onset. *NeuroImage*, 156, 286-292.  
<https://doi.org/10.1016/j.neuroimage.2017.05.017>

611 Genc, S., Smith, R. E., Malpas, C. B., Anderson, V., Nicholson, J. M., Efron, D., Sciberras, E., Seal, M.  
612 L., & Silk, T. J. (2018). Development of white matter fibre density and morphology over  
613 childhood: A longitudinal fixel-based analysis. *NeuroImage*, 183, 666-676.  
614 <https://doi.org/10.1016/j.neuroimage.2018.08.043>

615 Genc, S., Tax, C. M. W., Raven, E. P., Chamberland, M., Parker, G. D., & Jones, D. K. (2020). Impact  
616 of b-value on estimates of apparent fibre density. *Human Brain Mapping*, 41(10), 2583-  
617 2595. <https://doi.org/10.1002/hbm.24964>

618 Giedd, J. N., Blumenthal, J., Jeffries, N. O., Castellanos, F. X., Liu, H., Zijdenbos, A., Paus, T., Evans,  
619 A. C., & Rapoport, J. L. (1999). Brain development during childhood and adolescence: a  
620 longitudinal MRI study. *Nat Neurosci*, 2(10), 861-863. <https://doi.org/10.1038/13158>

621 Glasser, M. F., Sotiropoulos, S. N., Wilson, J. A., Coalson, T. S., Fischl, B., Andersson, J. L., Xu, J.,  
622 Jbabdi, S., Webster, M., Polimeni, J. R., Van Essen, D. C., & Jenkinson, M. (2013). The  
623 minimal preprocessing pipelines for the Human Connectome Project. *NeuroImage*, 80,  
624 105-124. <https://doi.org/10.1016/j.neuroimage.2013.04.127>

625 Gogtay, N., Giedd, J. N., Lusk, L., Hayashi, K. M., Greenstein, D., Vaituzis, A. C., Nugent, T. F.,  
626 Herman, D. H., Clasen, L. S., Toga, A. W., Rapoport, J. L., & Thompson, P. M. (2004).  
627 Dynamic mapping of human cortical development during childhood through early  
628 adulthood. *Proceedings of the National Academy of Sciences*, 101(21), 8174-8179.  
629 <https://doi.org/10.1073/pnas.0402680101>

630 Gomez, J., Barnett, M. A., Natu, V., Mezer, A., Palomero-Gallagher, N., Weiner, K. S., Amunts, K.,  
631 Zilles, K., & Grill-Spector, K. (2017). Microstructural proliferation in human cortex is  
632 coupled with the development of face processing. *Science*, 355(6320), 68-71.  
633 <https://doi.org/10.1126/science.aag0311>

634 Gomez, J., Natu, V., Jeska, B., Barnett, M., & Grill-Spector, K. (2018). Development differentially  
635 sculpts receptive fields across early and high-level human visual cortex. *Nature  
636 Communications*, 9(1), 788. <https://doi.org/10.1038/s41467-018-03166-3>

637 Gordon, E. M., Chauvin, R. J., Van, A. N., Rajesh, A., Nielsen, A., Newbold, D. J., Lynch, C. J.,  
638 Seider, N. A., Krimmel, S. R., Scheidter, K. M., Monk, J., Miller, R. L., Metoki, A., Montez, D.  
639 F., Zheng, A., Elbau, I., Madison, T., Nishino, T., Myers, M. J., Kaplan, S., Badke D'Andrea,  
640 C., Demeter, D. V., Feigelis, M., Ramirez, J. S. B., Xu, T., Barch, D. M., Smyser, C. D.,  
641 Rogers, C. E., Zimmermann, J., Botteron, K. N., Pruitt, J. R., Willie, J. T., Brunner, P.,  
642 Shimony, J. S., Kay, B. P., Marek, S., Norris, S. A., Gratton, C., Sylvester, C. M., Power, J. D.,  
643 Liston, C., Greene, D. J., Roland, J. L., Petersen, S. E., Raichle, M. E., Laumann, T. O., Fair,  
644 D. A., & Dosenbach, N. U. F. (2023). A somato-cognitive action network alternates with  
645 effector regions in motor cortex. *Nature*, 617(7960), 351-359.  
646 <https://doi.org/10.1038/s41586-023-05964-2>

647 Grayson, D. S., & Fair, D. A. (2017). Development of large-scale functional networks from birth to  
648 adulthood: A guide to the neuroimaging literature. *NeuroImage*, 160, 15-31.

649 Greve, D. N., & Fischl, B. (2009). Accurate and robust brain image alignment using boundary-  
650 based registration. *NeuroImage*, 48(1), 63-72.

651 Gu, S., Satterthwaite, T. D., Medaglia, J. D., Yang, M., Gur, R. E., Gur, R. C., & Bassett, D. S. (2015).  
652 Emergence of system roles in normative neurodevelopment. *Proceedings of the National  
653 Academy of Sciences*, 112(44), 13681-13686.

654 Hagmann, P., Kurant, M., Gigandet, X., Thiran, P., Wedeen, V. J., Meuli, R., & Thiran, J.-P. (2007).  
655 Mapping Human Whole-Brain Structural Networks with Diffusion MRI. *PLOS ONE*, 2(7),  
656 e597. <https://doi.org/10.1371/journal.pone.0000597>

657 Hermundstad, A. M., Bassett, D. S., Brown, K. S., Aminoff, E. M., Clewett, D., Freeman, S., Frithsen,  
658 A., Johnson, A., Tipper, C. M., Miller, M. B., Grafton, S. T., & Carlson, J. M. (2013).

659 Structural foundations of resting-state and task-based functional connectivity in the  
660 human brain. *Proceedings of the National Academy of Sciences*, 110(15), 6169-6174.  
661 <https://doi.org/10.1073/pnas.1219562110>

662 Herting, M. M., Kim, R., Uban, K. A., Kan, E., Binley, A., & Sowell, E. R. (2017). Longitudinal  
663 changes in pubertal maturation and white matter microstructure.  
664 *Psychoneuroendocrinology*, 81, 70-79. <https://doi.org/10.1016/j.psyneuen.2017.03.017>

665 Jenkinson, M., Bannister, P., Brady, M., & Smith, S. (2002). Improved optimization for the robust  
666 and accurate linear registration and motion correction of brain images. *NeuroImage*, 17(2),  
667 825-841.

668 Jeurissen, B., Leemans, A., Tournier, J. D., Jones, D. K., & Sijbers, J. (2013). Investigating the  
669 prevalence of complex fiber configurations in white matter tissue with diffusion magnetic  
670 resonance imaging. *Hum Brain Mapp*, 34(11), 2747-2766.  
671 <https://doi.org/10.1002/hbm.22099>

672 Jeurissen, B., Tournier, J. D., Dhollander, T., Connelly, A., & Sijbers, J. (2014). Multi-tissue  
673 constrained spherical deconvolution for improved analysis of multi-shell diffusion MRI  
674 data. *NeuroImage*, 103, 411-426. <https://doi.org/10.1016/j.neuroimage.2014.07.061>

675 Jones, D. K., Catani, M., Pierpaoli, C., Reeves, S. J., Shergill, S. S., O'Sullivan, M., Golesworthy, P.,  
676 McGuire, P., Horsfield, M. A., & Simmons, A. (2006). Age effects on diffusion tensor  
677 magnetic resonance imaging tractography measures of frontal cortex connections in  
678 schizophrenia. *Human Brain Mapping*, 27(3), 230-238.

679 Jones, D. K., Knösche, T. R., & Turner, R. (2013). White matter integrity, fiber count, and other  
680 fallacies: the do's and don'ts of diffusion MRI. *NeuroImage*, 73, 239-254.  
681 <https://doi.org/10.1016/j.neuroimage.2012.06.081>

682 Juraska, J. M., & Willing, J. (2017). Pubertal onset as a critical transition for neural development  
683 and cognition. *Brain Res*, 1654, 87-94.  
684 <https://doi.org/https://doi.org/10.1016/j.brainres.2016.04.012>

685 Kanaan, R. A., Shergill, S. S., Barker, G. J., Catani, M., Ng, V. W., Howard, R., McGuire, P. K., &  
686 Jones, D. K. (2006). Tract-specific anisotropy measurements in diffusion tensor imaging.  
687 *Psychiatry Research: Neuroimaging*, 146(1), 73-82.

688 Kellner, E., Dhital, B., Kiselev, V. G., & Reisert, M. (2016). Gibbs-ringing artifact removal based on  
689 local subvoxel-shifts. *Magn Reson Med*, 76(5), 1574-1581.  
690 <https://doi.org/10.1002/mrm.26054>

691 Khundrakpam, B. S., Reid, A., Brauer, J., Carbonell, F., Lewis, J., Ameis, S., Karama, S., Lee, J.,  
692 Chen, Z., Das, S., Evans, A. C., Brain Development Cooperative, G., Ball, W. S., Byars, A.  
693 W., Schapiro, M., Bommer, W., Carr, A., German, A., Dunn, S., Rivkin, M. J., Waber, D.,  
694 Mulkern, R., Vajapeyam, S., Chiverton, A., Davis, P., Koo, J., Marmor, J., Mrakotsky, C.,  
695 Robertson, R., McAnulty, G., Brandt, M. E., Fletcher, J. M., Kramer, L. A., Yang, G.,  
696 McCormack, C., Hebert, K. M., Volero, H., Botteron, K., McKinstry, R. C., Warren, W.,  
697 Nishino, T., Robert Almli, C., Todd, R., Constantino, J., McCracken, J. T., Levitt, J., Alger,  
698 J., O'Neil, J., Toga, A., Asarnow, R., Fadale, D., Heinichen, L., Ireland, C., Wang, D.-J., Moss,  
699 E., Zimmerman, R. A., Bintliff, B., Bradford, R., Newman, J., Evans, A. C., Arnaoutelis, R.,  
700 Bruce Pike, G., Louis Collins, D., Leonard, G., Paus, T., Zijdenbos, A., Das, S., Fonov, V., Fu,  
701 L., Harlap, J., Leppert, I., Milovan, D., Vins, D., Zeffiro, T., Van Meter, J., Lange, N.,  
702 Froimowitz, M. P., Botteron, K., Robert Almli, C., Rainey, C., Henderson, S., Nishino, T.,  
703 Warren, W., Edwards, J. L., Dubois, D., Smith, K., Singer, T., Wilber, A. A., Pierpaoli, C.,  
704 Basser, P. J., Chang, L.-C., Koay, C. G., Walker, L., Freund, L., Rumsey, J., Baskir, L.,  
705 Stanford, L., Sirocco, K., Gwinn-Hardy, K., Spinella, G., McCracken, J. T., Alger, J. R., Levitt,

706 J., & O'Neill, J. (2013). Developmental Changes in Organization of Structural Brain  
707 Networks. *Cerebral Cortex*, 23(9), 2072-2085. <https://doi.org/10.1093/cercor/bhs187>

708 Knudsen, E. I. (2004). Sensitive Periods in the Development of the Brain and Behavior. *Journal of*  
709 *Cognitive Neuroscience*, 16(8), 1412-1425. <https://doi.org/10.1162/0898929042304796>

710 Koenis, M. M., Brouwer, R. M., Swagerman, S. C., van Soelen, I. L., Boomsma, D. I., & Hulshoff Pol,  
711 H. E. (2018). Association between structural brain network efficiency and intelligence  
712 increases during adolescence. *Human Brain Mapping*, 39(2), 822-836.

713 LaMantia, A. S., & Rakic, P. (1990). Axon overproduction and elimination in the corpus callosum of  
714 the developing rhesus monkey. *J Neurosci*, 10(7), 2156-2175.  
<https://www.ncbi.nlm.nih.gov/pubmed/2376772>

715 Lebel, C., & Beaulieu, C. (2011). Longitudinal development of human brain wiring continues from  
716 childhood into adulthood. *J Neurosci*, 31(30), 10937-10947.  
<https://doi.org/10.1523/JNEUROSCI.5302-10.2011>

717 Lenroot, R. K., & Giedd, J. N. (2006). Brain development in children and adolescents: insights from  
718 anatomical magnetic resonance imaging. *Neuroscience & Biobehavioral Reviews*, 30(6),  
719 718-729.

720 Leppert, I. R., Bontempi, P., Rowley, C. D., Campbell, J. S. W., Nelson, M. C., Schiavi, S., Pike, G. B.,  
721 Daducci, A., & Tardif, C. L. (2023). Dual-encoded magnetization transfer and diffusion  
722 imaging and its application to tract-specific microstructure mapping. *Imaging*  
723 *Neuroscience*, 1, 1-17. [https://doi.org/10.1162/imag\\_a\\_00019](https://doi.org/10.1162/imag_a_00019)

724 Natu, V. S., Gomez, J., Barnett, M., Jeska, B., Kirilina, E., Jaeger, C., Zhen, Z., Cox, S., Weiner, K. S.,  
725 Weiskopf, N., & Grill-Spector, K. (2019). Apparent thinning of human visual cortex during  
726 childhood is associated with myelination. *Proceedings of the National Academy of*  
727 *Sciences*, 116(41), 20750-20759. <https://doi.org/10.1073/pnas.1904931116>

728 Palmer, C. E., Pecheva, D., Iversen, J. R., Hagler, D. J., Sugrue, L., Nedelec, P., Fan, C. C.,  
729 Thompson, W. K., Jernigan, T. L., & Dale, A. M. (2022). Microstructural development from  
730 9 to 14 years: Evidence from the ABCD Study. *Developmental Cognitive Neuroscience*,  
731 53, 101044. <https://doi.org/https://doi.org/10.1016/j.dcn.2021.101044>

732 Panagiotaki, E., Schneider, T., Siow, B., Hall, M. G., Lythgoe, M. F., & Alexander, D. C. (2012).  
733 Compartment models of the diffusion MR signal in brain white matter: a taxonomy and  
734 comparison. *NeuroImage*, 59(3), 2241-2254.

735 Paus, T. (2010). Growth of white matter in the adolescent brain: myelin or axon? *Brain Cogn*,  
736 72(1), 26-35. <https://doi.org/10.1016/j.bandc.2009.06.002>

737 Rubinov, M., & Sporns, O. (2010). Complex network measures of brain connectivity: uses and  
738 interpretations. *NeuroImage*, 52(3), 1059-1069.

739 Rudrapatna, U., Parker, G. D., Roberts, J., & Jones, D. K. (2021). A comparative study of gradient  
740 nonlinearity correction strategies for processing diffusion data obtained with ultra-strong  
741 gradient MRI scanners. *Magn Reson Med*, 85(2), 1104-1113.  
<https://doi.org/10.1002/mrm.28464>

742 Sairanen, V., Leemans, A., & Tax, C. M. (2018). Fast and accurate Slicewise OutLlier Detection  
743 (SOLID) with informed model estimation for diffusion MRI data. *NeuroImage*, 181, 331-  
744 346.

745 Schiavi, S., Lu, P.-J., Weigel, M., Lutti, A., Jones, D. K., Kappos, L., Granziera, C., & Daducci, A.  
746 (2022). Bundle myelin fraction (BMF) mapping of different white matter connections using  
747 microstructure informed tractography. *NeuroImage*, 249, 118922.  
<https://doi.org/https://doi.org/10.1016/j.neuroimage.2022.118922>

748 Schiavi, S., Ocampo-Pineda, M., Barakovic, M., Petit, L., Descoteaux, M., Thiran, J.-P., & Daducci,  
749 A. (2020). A new method for accurate in vivo mapping of human brain connections using

750

751

752

753

754 microstructural and anatomical information. *Science Advances*, 6(31), eaba8245.  
755 <https://doi.org/10.1126/sciadv.aba8245>

756 Schiavi, S., Petracca, M., Battocchio, M., El Mendili, M. M., Paduri, S., Fleysher, L., Inglese, M., &  
757 Daducci, A. (2020). Sensory-motor network topology in multiple sclerosis: Structural  
758 connectivity analysis accounting for intrinsic density discrepancy. *Human Brain Mapping*,  
759 41(11), 2951-2963. <https://doi.org/https://doi.org/10.1002/hbm.24989>

760 Schilling, K. G., Tax, C. M. W., Rheault, F., Landman, B. A., Anderson, A. W., Descoteaux, M., &  
761 Petit, L. (2022). Prevalence of white matter pathways coming into a single white matter  
762 voxel orientation: The bottleneck issue in tractography. *Human Brain Mapping*, 43(4),  
763 1196-1213. <https://doi.org/https://doi.org/10.1002/hbm.25697>

764 Seguin, C., Razi, A., & Zalesky, A. (2019). Inferring neural signalling directionality from undirected  
765 structural connectomes. *Nature Communications*, 10(1), 4289.

766 Seguin, C., Sporns, O., & Zalesky, A. (2023). Brain network communication: concepts, models and  
767 applications. *Nature reviews neuroscience*, 24(9), 557-574.  
768 <https://doi.org/10.1038/s41583-023-00718-5>

769 Smith, R., Raffelt, D., Tournier, J.-D., & Connelly, A. (2020). Quantitative streamlines tractography:  
770 methods and inter-subject normalisation.

771 Smith, S. M., Jenkinson, M., Woolrich, M. W., Beckmann, C. F., Behrens, T. E., Johansen-Berg, H.,  
772 Bannister, P. R., De Luca, M., Dobrajnik, I., & Flitney, D. E. (2004). Advances in functional  
773 and structural MR image analysis and implementation as FSL. *NeuroImage*, 23, S208-  
774 S219.

775 Suárez, L. E., Markello, R. D., Betzel, R. F., & Misic, B. (2020). Linking structure and function in  
776 macroscale brain networks. *Trends in cognitive sciences*, 24(4), 302-315.

777 Tamnes, C. K., Roalf, D. R., Goddings, A. L., & Lebel, C. (2018). Diffusion MRI of white matter  
778 microstructure development in childhood and adolescence: Methods, challenges and  
779 progress. *Dev Cogn Neurosci*, 33, 161-175. <https://doi.org/10.1016/j.dcn.2017.12.002>

780 Tournier, J.-D., Smith, R., Raffelt, D., Tabbara, R., Dhollander, T., Pietsch, M., Christiaens, D.,  
781 Jeurissen, B., Yeh, C.-H., & Connelly, A. (2019). MRtrix3: A fast, flexible and open software  
782 framework for medical image processing and visualisation. *NeuroImage*, 202, 116137.

783 Tournier, J. D., Calamante, F., & Connelly, A. (2010). Improved probabilistic streamlines  
784 tractography by 2nd order integration over fibre orientation distributions. *Proceedings of  
785 the international society for magnetic resonance in medicine*,

786 Tustison, N. J., Avants, B. B., Cook, P. A., Zheng, Y., Egan, A., Yushkevich, P. A., & Gee, J. C.  
787 (2010). N4ITK: improved N3 bias correction. *IEEE Trans Med Imaging*, 29(6), 1310-1320.  
788 <https://doi.org/10.1109/tmi.2010.2046908>

789 Van den Heuvel, M. P., & Sporns, O. (2013). Network hubs in the human brain. *Trends in cognitive  
790 sciences*, 17(12), 683-696.

791 Veraart, J., Fieremans, E., & Novikov, D. S. (2016). Diffusion MRI noise mapping using random  
792 matrix theory. *Magnetic Resonance in Medicine*, 76(5), 1582-1593.

793 Vos, S. B., Tax, C. M., Luijten, P. R., Ourselin, S., Leemans, A., & Froeling, M. (2017). The  
794 importance of correcting for signal drift in diffusion MRI. *Magnetic Resonance in Medicine*,  
795 77(1), 285-299.

796 Wandell, B. A. (1999). COMPUTATIONAL NEUROIMAGING OF HUMAN VISUAL CORTEX.  
797 *Annual Review of Neuroscience*, 22(1), 145-173.  
798 <https://doi.org/10.1146/annurev.neuro.22.1.145>

799 Ward, I. L., Raven, E. P., de la Rosa, S., Jones, D. K., Teufel, C., & von dem Hagen, E. (2023). White  
800 matter microstructure in face and body networks predicts facial expression and body

801 posture perception across development. *Human Brain Mapping*, 44(6), 2307-2322.  
802 <https://doi.org/https://doi.org/10.1002/hbm.26211>

803 Yakovlev, P. I., & Lecours, A. R. (1967). *The myelogenetic cycles of regional maturation of the*  
804 *brain*. F. A. Davis Company, Philadelphia, Pa. <Go to  
805 ISI>://BIOSIS:PREV19674800116606

806 Yeh, C. H., Jones, D. K., Liang, X., Descoteaux, M., & Connelly, A. (2021). Mapping structural  
807 connectivity using diffusion MRI: Challenges and opportunities. *Journal of Magnetic*  
808 *Resonance Imaging*, 53(6), 1666-1682.

809 Yeo, B. T., Krienen, F. M., Sepulcre, J., Sabuncu, M. R., Lashkari, D., Hollinshead, M., Roffman, J. L.,  
810 Smoller, J. W., Zöllei, L., Polimeni, J. R., Fischl, B., Liu, H., & Buckner, R. L. (2011). The  
811 organization of the human cerebral cortex estimated by intrinsic functional connectivity. *J*  
812 *Neurophysiol*, 106(3), 1125-1165. <https://doi.org/10.1152/jn.00338.2011>

813 Zhang, F., Daducci, A., He, Y., Schiavi, S., Seguin, C., Smith, R. E., Yeh, C.-H., Zhao, T., &  
814 O'Donnell, L. J. (2022). Quantitative mapping of the brain's structural connectivity using  
815 diffusion MRI tractography: A review. *NeuroImage*, 249, 118870.

816

817 8. Supplementary  
818 8.1. Tables

821 **Table S1:** Diffusivity parameters estimated in a white matter mask for one younger (8-year-old)  
822 and one older (17-year-old) participant. Values are reported as mean (SD).

	$d_a$	$d_{par}$	$d_{perp}$
Younger	2.27 (0.71)	2.01 (0.57)	0.61 (0.28)
Older	2.35 (0.62)	1.71 (0.58)	0.62 (0.27)

824  
825  
826  
827 **Table S2:** Regions from the Destrieux parcellation assigned to each canonical cortical network.  
828 Results for left hemisphere shown (equivalent in right hemisphere). Only nodes overlapping the  
829 same network in >80% of participants were included in the analysis.

Region	Name	X	Y	Z	C	Yeo7_name	N
2	G_and_S_occipital_inf	23	60	180	255	visual	88
3	G_and_S_paracentral	63	100	60	255	somatomotor	87
4	G_and_S_subcentral	63	20	220	255	somatomotor	88
5	G_and_S_transv_frontopol	13	0	250	255	dmn	88
6	G_and_S_cingul-Ant	26	60	0	255	dmn	88
7	G_and_S_cingul-Mid-Ant	26	60	75	255	ventralattention	88
9	G_cingul-Post-dorsal	25	60	250	255	dmn	88
10	G_cingul-Post-ventral	60	25	25	255	dmn	88
11	G_cuneus	180	20	20	255	visual	88
12	G_front_inf-Opercular	220	20	100	255	ventralattention	86
13	G_front_inf-Orbital	140	60	60	255	dmn	88
15	G_front_middle	140	100	180	255	frontoparietal	84
16	G_front_sup	180	20	140	255	dmn	88
17	G_Ins_lg_and_S_cent_ins	23	10	10	255	ventralattention	88
18	G_insular_short	225	140	140	255	ventralattention	88
19	G_occipital_middle	180	60	180	255	visual	88
20	G_occipital_sup	20	220	60	255	visual	88
21	G_oc-temp_lat-fusifor	60	20	140	255	visual	88
22	G_oc-temp_med-Lingual	220	180	140	255	visual	88
23	G_oc-temp_med-Parahip	65	100	20	255	limbic	88
24	G_orbital	220	60	20	255	limbic	80
25	G_pariet_inf-Angular	20	60	220	255	dmn	88
26	G_pariet_inf-Supramar	100	100	60	255	ventralattention	84
27	G_parietal_sup	220	180	220	255	dorsalattention	88
28	G_postcentral	20	180	140	255	somatomotor	87
29	G_precentral	60	140	180	255	somatomotor	88
31	G_rectus	20	60	100	255	limbic	88
32	G_subcallosal	60	220	20	255	limbic	88
33	G_temp_sup-G_T_transv	60	60	220	255	somatomotor	88
35	G_temp_sup-Plan_polar	65	220	60	255	limbic	88

38	G_temporal_middle	180	60	60	255	dmn	88
41	Lat_Fis-post	61	60	100	255	somatomotor	88
42	Pole_occipital	140	20	60	255	visual	88
43	Pole_temporal	220	180	20	255	limbic	88
44	S_calcarine	63	180	180	255	visual	88
45	S_central	221	20	10	255	somatomotor	87
46	S_cingul-Marginalis	221	20	100	255	ventralattention	84
48	S_circular_insula_inf	221	20	220	255	ventralattention	86
49	S_circular_insula_sup	61	220	220	255	ventralattention	88
50	S_collat_transv_ant	100	200	200	255	limbic	88
51	S_collat_transv_post	10	200	200	255	visual	88
52	S_front_inf	221	220	20	255	frontoparietal	88
56	S_intrapariet_and_P_trans	143	20	220	255	dorsalattention	84
57	S_oc_middle_and_Lunatus	101	60	220	255	visual	88
58	S_oc_sup_and_transversal	21	20	140	255	visual	88
60	S_oc-temp_lat	221	140	20	255	dorsalattention	87
61	S_oc-temp_med_and_Lingual	141	100	220	255	visual	88
62	S_orbital_lateral	221	100	20	255	frontoparietal	77
63	S_orbital_med-olfact	181	200	20	255	limbic	88
65	S_parieto_occipital	101	100	180	255	visual	85
69	S_precentral-sup-part	21	20	200	255	dorsalattention	86
71	S_subparietal	101	60	60	255	dmn	88
73	S_temporal_sup	223	220	60	255	dmn	88
74	S_temporal_transverse	221	60	60	255	somatomotor	88
76	Left-Thalamus-Proper	0	118	14	255	subcortical	88
77	Left-Caudate	122	186	220	255	subcortical	88
78	Left-Putamen	236	13	176	255	subcortical	88
79	Left-Pallidum	12	48	255	255	subcortical	88
80	Left-Hippocampus	220	216	20	255	subcortical	88
81	Left-Amygdala	103	255	255	255	subcortical	88
82	Left-Accumbens-area	255	165	0	255	subcortical	88

832 **Table S3:** Results of mixed-effect model selection for first level global graph network analysis.

833 Values reported are Akaike Information Criterion (AIC) of each model fit.

834

Model	Modularity	Global Efficiency	Clustering Coefficient	Mean Strength
M1a	-2816.78	-2549.70	-3792.68	244.49
M2a	-2821.03	-2553.69	-3796.30	237.85
M3a	-2832.02	-2565.74	-3795.91	167.79
M4a	-2860.55	-2575.29	-3814.42	90.46
M1b	-2825.11	-2569.99	-3801.41	215.66
M2b	-2826.42	-2570.17	-3802.19	214.00
M3b	-2840.35	-2586.03	-3804.65	138.97
M4b	<b>-2865.94*</b>	<b>-2591.77*</b>	<b>-3820.31*</b>	<b>66.60*</b>

835 Note: Bold indicates lowest AIC for each graph measure; \* indicates if the age by network term  
836 was significant at p<.005

837

838 Footnote: Models tested are as follows:

839 M1a <- lmer(measure ~ age + sex + network + (1|ID), REML=FALSE, data=data)

840 M2a <- lmer(measure ~ age \* sex + network + (1|ID), REML=FALSE, data=data)

841 M3a <- lmer(measure ~ age \* network + sex + (1|ID), REML=FALSE, data=data)

842 M4a <- lmer(measure ~ age \* sex \* network + (1|ID), REML=FALSE, data=data)

843 M1b <- lmer(measure ~ age + sex + network + ICV + (1|ID), REML=FALSE, data=data)

844 M2b <- lmer(measure ~ age \* sex + network + ICV + (1|ID), REML=FALSE, data=data)

845 M3b <- lmer(measure ~ age \* network + sex + ICV + (1|ID), REML=FALSE, data=data)

846 M4b <- lmer(measure ~ age \* sex \* network + ICV + (1|ID), REML=FALSE, data=data)

847 **Table S4:** Results from comparison of age-associations of graph measures with reference to the  
 848 visual network. Bold values indicate networks which have significantly different slopes to the age-  
 849 relationship in the visual network, generated using linear mixed effects models.  
 850

Network	Global efficiency		Clustering coefficient		Mean strength	
	t	p-value	t	p-value	t	p-value
<i>Visual (reference)</i>						
Default mode	-1.65	.10	-2.91	<b>.004</b>	-4.08	<b>5E-05</b>
Dorsal attention	-2.96	<b>.003</b>	-1.17	.24	-5.25	<b>2E-07</b>
Fronto-parietal	-1.64	.10	-1.66	.10	-3.91	<b>1E-04</b>
Limbic	-2.04	.04	-1.87	.06	-4.01	<b>7E-05</b>
Somatomotor	-0.60	.55	-1.16	.25	-1.78	.08
Subcortical	-2.19	.03	-2.19	.03	-4.55	<b>6E-06</b>
Ventral attention	-1.93	.05	-3.05	<b>.002</b>	-4.34	<b>2E-05</b>
<i>Somatomotor (reference)</i>						
Default mode	-1.05	.29	-1.05	.29	-2.30	.02
Dorsal attention	-2.36	.02	-2.36	.02	-3.48	<b>&lt;.001</b>
Fronto-parietal	-1.04	.30	-1.04	.30	-2.13	.03
Limbic	-1.45	.15	-1.45	.15	-2.23	.03
Subcortical	-1.60	.11	-1.60	.11	-2.78	.006
Ventral attention	-1.33	.18	-1.33	.18	-2.56	.011
Visual	0.60	.55	0.60	.55	1.78	.08

851 Note: model used was the best fitting model deduced from Table S3.